Comparison of flow characteristics around an equilateral triangular cylinder via PIV and Large Eddy Simulation methods

Sercan Yagmur, Sercan Dogan, Muharrem Hilmi Aksoy, Ilker Goktepeli*, Muammer Ozgoren

Selcuk University, Faculty of Engineering, Department of Mechanical Engineering, 42075 Selcuklu, Konya, Turkey

ABSTRACT

The flow structures around an equilateral triangular cylinder, which is commonly used as a vortex shedder in the vortex flowmeter, were investigated experimentally and numerically. Flow characteristics such as vorticity contours, patterns of sectional streamlines, velocity vectors, velocity fields, Reynolds stress correlations, Strouhal numbers and drag coefficients were examined using the Particle Image Velocimetry (PIV) technique and the Large Eddy Simulation (LES) turbulence model. Experimental studies were performed in an open water channel for $Re = 2.9 \times 10^3$, $Re = 5.8 \times 10^3$ and $Re = 1.16 \times 10^4$ based on the equilateral triangle edge. A sharp-tip corner of the cylinder with a triangle cross-section was exposed to the upstream side while the other two sharp-tip corners were placed on the downstream side. Numerical studies were also completed at Reynolds numbers in the range of $2.9 \times 10^3 \le Re \le 1.16 \times 10^5$ to obtain the changes in the Strouhal numbers and drag coefficients. When the results of PIV and LES are considered in the same interval of Reynolds numbers, the maximum and minimum values of each flow pattern were nearly the same. The time-averaged patterns had considerable symmetry with respect to the axis line passing through the sharp-tip corner of the cross-section of the triangular cylinder. The Strouhal number was independent of the Reynolds number and was found to be approximately 0.22. The drag coefficient decreased with increasing Reynolds numbers while increasing the Power Spectral Density (PSD) and the vortex shedding frequency. For the same Reynolds numbers, the experimental and numerical results were in good agreement. Therefore, the LES turbulence model is recommended for applications of flow around this type of bluff body that is generally used in the design of vortex flowmeters to generate vortex shedding.

1. Introduction

Fluid flow around bluff bodies (e.g., circular, rectangular, triangular cross-sectional cylinders) has been studied by researchers for centuries because of its importance in various engineering applications such as flow measurements, electronic cooling, heat exchanger systems, bridge piers, high-rise buildings, flow dividers, sensors and probes among other applications [1]. One of these industrial application areas is the flow measurement by vortex flowmeters that could be used independently of the fluid phase. The fundamental working principle of these instruments is the measurement of the vortex shedding frequency, which is referred to as von Karman Vortex Street in the wake region of bluff bodies. As the vortex shedding frequency and free stream velocity change proportionally like the von Karman Vortex Street, the Strouhal number remains constant [2].

Various methods are used for the vortex flowmeter to determine the flow rate. A well-known method includes pressure sensors near the wake of the bluff body to obtain the vortex frequency. To generate vortex shedding in a vortex flowmeter, different cross-sectional cylinders and their various arrangements have been used for decades. For generating better vortex shedding, because of sharp corners, a prismatic cross-sectional cylinder is preferred to a circular cylinder. For instance, Ozgoren [3] investigated flow characteristics of flow around circular, square and oriented square cylinders at a 45° orientation by using Particle Image Velocimetry (PIV) techniques at $550 \le Re \le 3.4 \times 10^3$. The author obtained Strouhal numbers such as $St = 0.204$–0.212 for the circular cylinder, $St = 0.12$–0.134 for the square cylinder and $St = 0.165$–0.174 for the oriented square cylinder at $550 \le Re \le 3.4 \times 10^3$. It was concluded that the values of the vortex shedding frequency were nearly same. However, the peak frequencies of the Power Spectral Density (PSD) changed with the cross-sections of the cylinder. In a water tank, Okajima [4] experimentally investigated the flow around the square and the rectangular cylinders for $70 \le Re \le 2 \times 10^4$ to define the vortex shedding frequencies and the corresponding Strouhal numbers. At values higher than $Re = 10^4$, the Strouhal number was not the function of the Reynolds number.

However, the cross-section of the cylinder was the function of the Strouhal number, and the cross-section varied with the width-to-height ratio of the cylinder. Knauss et al. [5] measured the vortex shedding frequency in the wake region of elliptical and square cylinders. They determined that the Strouhal number depended on the geometrical shape of the bluff body, and the Strouhal number was almost not influenced by the Reynolds number. Yen and Yang [6] studied the flow over a square cylinder in the range of $4 \times 10^3 \leq Re \leq 3.6 \times 10^4$ with incidence angles of $0° \leq \theta \leq 45°$. The minimum and maximum Strouhal numbers occurred at $\theta = 0°$ and $\theta = 15°$, respectively. Another experimental study on the comparison of flow characteristics of circular cylinder and sphere was performed by Ozgoren et al. [7] at $Re = 5 \times 10^3$ and $Re = 10 \times 10^3$. They concluded that the wake flow of the sphere was more complex than the wake flow of the circular cylinder because of the 3-D flow. The vortex shedding frequency of the sphere was found to be higher than the vortex shedding frequency of the circular cylinder, but the PSD of the sphere was lower than the PSD of the circular cylinder. In addition to these studies, various investigations of the circular and square cylinders were experimentally performed by Huang et al. [8], Gu et al. [9], Lee and Lee [10], Kalmbach and Breuer [11] and Gunes et al. [12]. They considered the effect of geometry and flow control method on the vortex shedding frequency in their studies.

However, investigation of the vortex shedding frequency and flow characteristics over bluff bodies is a common research field in fluid mechanics, but limited studies of the flow around triangular cross-sectional cylinder-like bodies have been performed. Agrawal et al. [13], El-Sherbiny [14] and Iungo and Buresti [15] determined the flow characteristics of different orientations affecting a triangular prism using various experimental flow visualization techniques. They decided that the apex angle influenced the vortex shedding frequency and the Strouhal number. Another experimental study of the flow over a dual triangulate body in a circular pipe was performed by Peng et al. [16] to investigate the Strouhal number by using a piezoelectric sensor to acquire the vortex shedding frequency. The Strouhal numbers changed with the distance between the two bluff bodies. As a result, the Reynolds number did not have very much effect on the Strouhal number. A study of the vortex shedding frequency of a triangular cylinder was completed by Zhang et al. [17] to investigate the effect of the fluid type on the Strouhal number at the same Reynolds number. The Strouhal number was found to be nearly the same for water and air at the same Reynolds number and the Strouhal number was not affected by the Reynolds number in the same manner as the circular and different cross-sectional cylinders. However, the PSD and vortex shedding frequency were higher when air was chosen as the fluid because of the high velocity required to provide Reynolds number equality.

Due to reliable results with better validation performance between experimental and numerical studies in recent years, Computational Fluid Dynamics (CFD) has been used in a wide range of research areas as an alternative to experimental and analytical studies. For example, experimental and numerical studies on the comparison of a triangular cylinder with trapezoidal and other cross-sectional cylinders were performed by Cheng and Liu [18] and Venugopal et al. [19]. Both studies stated that the experimental results were in good agreement with the numerical results, and the vortex shedding frequency of a trapezoidal cross-sectional cylinder was higher than the vortex shedding frequency of a triangular cylinder. Zhang and Blair [2] compared the flow characteristics and the Strouhal number around a triangular cylinder via experimental and CFD results at $Re = 4.5 \times 10^4$, and they decided that experimental and numerical results indicated a close agreement with ± 2.7% relative error. Khaledi and Andersson [20] performed a numerical investigation of the vortex shedding from face and corner orientations of a hexagonal cylinder at $100 \leq Re \leq 10^3$. They stated that the corner orientation provided lower Strouhal numbers. Although the Strouhal number increased from $Re = 100$ to $Re = 500$, the Strouhal number remained constant from $Re = 500$ to $Re = 10^3$. As

accepted by the literature, CFD is a useful method for a design process and significantly improves the efficiency of newly designed and manufactured industrial products. Furthermore, CFD analysis is a cheaper and more effective way to ensure precise quantitative output into the aerodynamic and hydrodynamic flow characteristics of flow around a bluff body [21,22].

The overall objective of the present investigation is to visualize flow characteristics and obtain the vortex shedding frequency in the wake of a triangular cross-sectional cylinder model via PIV technique and the CFD method using a LES turbulence model in ANSYS-Fluent. The LES turbulence model has been used in the literature because the LES turbulence model yielded results similar with respect to the experimental results in some different fluid flow applications presented by Hassanzadeh et al. [23], Gang et al. [24], Luo et al. [25] and Zhang et al. [26]. Although many experimental and numerical studies about the flow over bluff bodies have been performed, it is difficult to locate detailed studies of the flow characteristics and spectral analysis of a horizontal axis triangular cylinder in the literature comparing PIV and the LES turbulence model. This situation has motivated us to investigate the flow across an equilateral triangular cylinder in a steady flow regime. The main aim of this study was to confirm the numerical LES turbulence model results with compared to the experimental results in terms of the vortex shedding frequency to contribute to the measurement principle of the vortex flowmeters, instantaneous and time-averaged flow patterns by using the PIV technique and the LES turbulence model at $Re = 2.9 \times 10^3$, $Re = 5.8 \times 10^3$ and $Re = 1.16 \times 10^4$. Furthermore, the concurrence between the results of PIV and LES leads us to obtain the Strouhal numbers independently of the Reynolds number and the variation in the drag coefficient. For this reason, the range for the Reynolds numbers was expanded to $Re = 1.16 \times 10^5$ for the numerical studies.

2. Methods

2.1. PIV measurement

Experiments were carried out in a large-scale open water channel with a rectangular cross-section and the dimensions of 770 mm × 600 mm × 6000 mm for width, height and length in the Advanced Technology Research and Application Center of Selcuk University in Turkey. The PIV system is depicted schematically in Fig. 1. To simplify laser transmission and flow visualization, test-section walls were constructed from 15 mm thick transparent glass plates, and the tank was filled with water to a level of $h_w = 475$ mm. The water was pumped by a centrifugal pump controlled with a frequency converter, and before reaching the test section, the water passed through a honeycomb section and a two-to-one channel contraction. The uncertainty of free-stream turbulence intensity was less than 1% in the range of the current Reynolds numbers, $Re = (U_\infty \ L)/\nu$, based on the characteristic edge. Here, L is the side edge of the equilateral triangular cylinder, ν is the kinematic viscosity and U_∞ is the free-stream velocity varied from 58 mm/s to 232 mm/s. The triangle was made from acrylic glass with an edge dimension of 50 mm and a 5 mm wall thickness. The triangle is a hollow, and it is filled with water to diminish the laser sheet deflection and highly polished to avoid surface roughness. The length of the triangle cross-section cylinder is 600 mm. The Nd: YAG laser with a maximum of 15 Hz was used to generate a laser sheet perpendicular to the axis of the cylinder. The thickness of the laser sheet was approximately 1 mm. The 10 μm-diameter suspended seeding particles in the flow were silver-coated hollow glass spheres. The equilateral triangular cylinder is horizontally located at the middle section of the water channel between two walls to avoid surface and wall effects from the channel. Moreover, to fulfill the high-image density criterion, the interrogation area contains nearly 20–30 particles per image. A Complementary Metal–Oxide–Semiconductor (CMOS) camera with a resolution of 1632 × 1200 pixels was used to capture
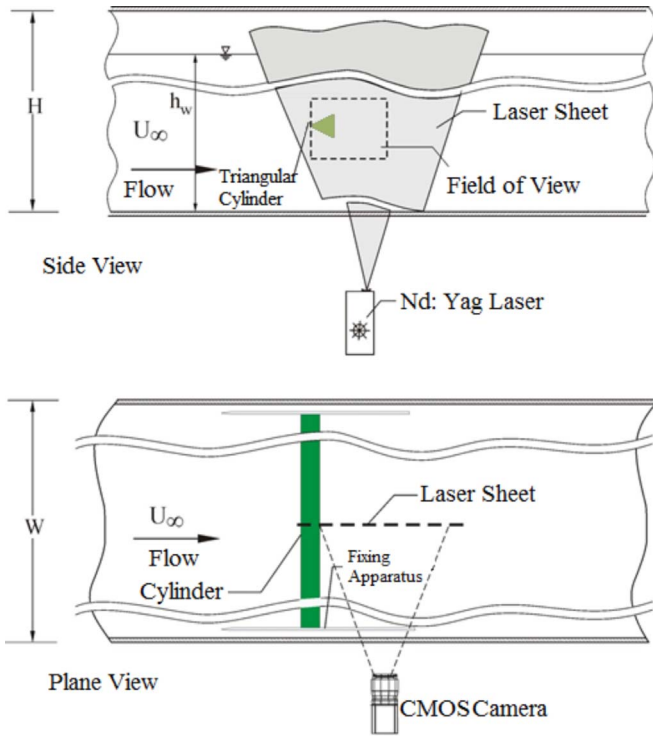
Fig. 1. Schematic view of the PIV system experimental setup, with laser illumination for an equilateral triangular cylinder located in a uniform flow condition.

2048 instantaneous image pairs at the rate of 15 Hz to calculate 1024 vector fields.

An interrogation window of 32×32 pixels for each image was selected and converted to approximately 1.41×1.41 mm^2 grid size ($0.028L \times 0.028L$) with adaptive correlations consisting of 7474 (101×74) velocity vectors. During the adaptive-correlation process, an overlap of 50% was used for all interrogation areas to satisfy the Nyquist criterion. From instantaneous velocity vector fields, the time-averaged flow patterns were calculated. For the post processing, Dantec Dynamic Studio software was employed including proper filters to compute the raw displacement vector field from the particle image data.

As explained by Ozgoren [3], the seeding particle size, particle overlap, non-uniform particle distribution, unmatched particle correlations, out of laser plane motion bias and random errors, interrogation window size, and electronic and optical imaging noise were the main uncertainty factors for velocity measurement and vorticity calculation in the PIV method. In the uncertainty evaluation of the velocity measurement, the influence of these factor calculations was determined to be in the range of ± 2–5%, and for detailed information, the studies of Ozgoren [3], Adrian [27], Fouras and Soria [28], and Hart [29] can be examined.

2.2. Large Eddy Simulation (LES)

2.2.1. Mathematical models

For the numerical studies, the turbulent characteristics have been computed in various ways in the literature. In this study, the LES turbulence model, which has been associated with the ANSYS-Fluent software package, was used to simulate the flow field around the equilateral triangular cylinder. The governing equations for an incompressible flow form of the continuity and the Reynolds Averaged Navier-Stokes equations are specified as follows [30]:

$$\frac{\partial \overline{u}_i}{\partial x_i} = 0 \tag{1}$$

$$\frac{\partial \overline{u}_i}{\partial t} + \frac{\partial \overline{u}_i \overline{u}_j}{\partial x_j} = \frac{1}{\rho} \frac{\partial \overline{p}}{\partial x_i} - \frac{\partial \tau_{ij}}{\partial x_j} + v \frac{\partial^2 \overline{u}_i}{\partial x_i \partial x_j} \tag{2}$$

where u_i is the filtered velocity component along the Cartesian coordinates x_i, ρ is the density of fluid and p is the pressure. The main principle of the LES is low-pass filtering. When this operation is applied to the Navier–Stokes equations, large-scale eddies are computed directly, whereas the small scale eddies are modeled using a sub-grid scale (SGS) model.

The influence of the small scales on the large (resolved) scales takes place through the sub-grid scale stress as given by [30]:

$$\tau_{ij} = \rho(\overline{u_i u_j} - \overline{u}_i \overline{u}_j) \tag{3}$$

resulting from the filtering operation, which is unknown and must be modeled with a sub-grid scale model (SGS) occurring in several sub-models. SGS is based on the eddy viscosity approach and is defined by [30]:

$$\tau_{ij} - \frac{1}{3}\tau_{kk}\delta_{ij} = -2\mu_t \overline{S}_{ij} \tag{4}$$

where the trace of the sub-grid scale stresses τ_{kk} is incorporated into the pressure resulting in a filtered isotropic pressure term; μ_t is the sub-grid-scale turbulent viscosity, and $\overline{S}_{ij}$ is the resolved scale of the strain rate tensor and described by [30]:

$$\overline{S}_{ij} = \frac{1}{2}\left(\frac{\partial \overline{u}_i}{\partial x_j} + \frac{\partial \overline{u}_j}{\partial x_i}\right) \tag{5}$$

The simplest and well-known sub-grid scale models are the Smagorinsky and later Lilly models. In both of these models, the eddy-viscosity is characterized as [30]:

$$\mu_t = \rho L_s^2 |\overline{S}_{ij}| \tag{6}$$

In Eq. (6), L_s is the length of mixing for the sub-grid scales, and when the resolved scale of the strain rate tensor is defined by Eq. (7) [30]:

$$|\overline{S}_{ij}| = \sqrt{\overline{S}_{ij}\overline{S}_{ij}} L_s \tag{7}$$

The mixing length for the sub-grid scales is computed as [30]:

$$L_s = \min\left(\kappa, d, C_s V^{1/3}\right) \tag{8}$$

In this equation, κ is the von Karman constant, d is the interval to the closest wall, C_s is the Smagorinsky constant, and V is the computational cell volume [30].

2.2.2. Computational domain and boundary conditions

In the present study, the computational 3-D water flow domain was prepared by considering the PIV measurement field. The center of the flow domain was set at the sharp-tip of the triangle cross-section. The flow domain dimensions are $-6.0L \leq x \leq 24.0L$ in the streamwise direction, $-4.75L \leq y \leq 4.75L$ in the vertical direction and $-6.0L \leq z \leq 6.0L$ in the transverse direction, as shown in Fig. 2.

On the surfaces of the solid model, a no-slip boundary condition is defined, and the pressure is set to zero. At the inlet boundary condition, the velocity inlet is described with a uniform velocity and zero pressure
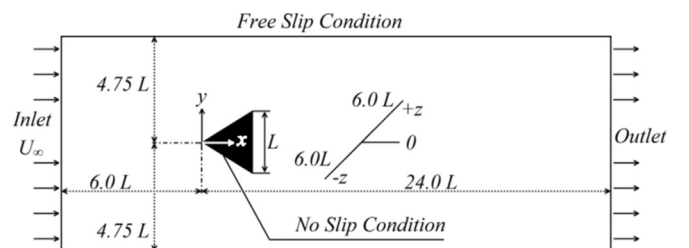

Fig. 2. Flow domain and boundary conditions in the present study.
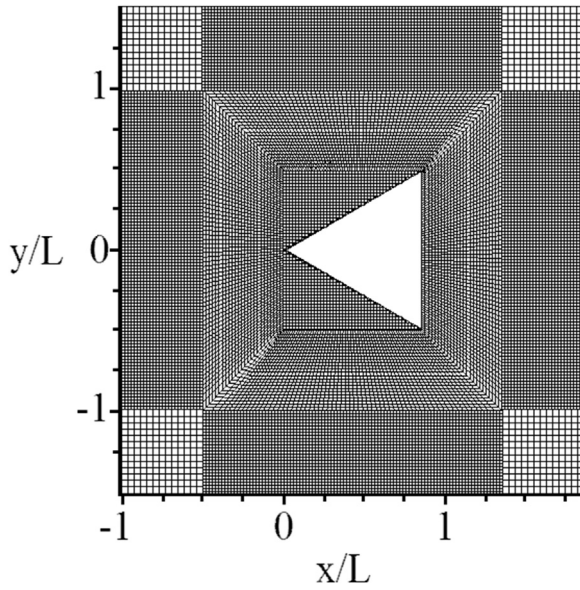
Fig. 3. Non-uniform grid structure near the body surface on the *x-y* plane.

gradients. At the outlet boundary condition, the pressure outlet is specified as zero. At the top, bottom and side boundaries, the free-slip conditions are implemented. The finite volume method is integrated to solve the transient incompressible Navier–Stokes equation with the pressure and velocity coupling with the splitting of the coupled-type algorithm. In the LES turbulence model, physical diffusion is remarkably affected by numerical diffusion; consequently, the central differencing schemes should be a suitable approach to conduct the spatial discretization. Therefore, the second order implicit scheme was selected for pressure and momentum spatial discretization with the Green-Gauss solver. For time integration bounded central differencing format is used [24,25,31–35]. For the transient analyses, to match PIV frequency, a constant time step $\Delta t = 0.066$ s was specified during the solution with 20 sub-iterations for each step. In addition, the convergence of each step was less than 10^{-6} for all equations to be solved.

2.2.3. Mesh arrangement

The flow domain is known to require enough grids to solve a complex flow structure. The non-uniform grid structure in the vicinity of the equilateral triangular cylinder is shown in Fig. 3. Considering the duration of the analyses and the computing capacity, the flow domain was divided into parts. To determine the shear layer effect and flow characteristics in detail, the finer grids were built near the face and wake region of the equilateral triangular cylinder. Grid size coarser than a critical value is not able to capture local variations of the model and flow domain on scales greater than the element size. Thus, the time-averaged simulation results of the LES model do not coincide with experimental results even though convergence is occurring. For these reasons, a grid independence study was completed by examining effects of the mesh density on the value of the mean drag force coefficients. In identifying the regular and irregular forces acting on the body, flow characteristics play an important role. These types of forces can cause structural damage. One of these forces is the drag force that is acting on the bluff body in the streamwise direction, and the drag force can be expressed by the dimensionless drag coefficient as follows:

$$C_D = \frac{2F_D}{\rho U_\infty^2 A} \tag{9}$$

where F_D is the drag force in the streamwise direction, ρ is fluid density and A is the projection area of the front view. The drag coefficient is shown to be changing with the grid number in Table 1. With an increasing grid number, the difference is decreasing at the same

Table 1
Grid independence study on the drag coefficient (C_D) at Re $= 1.16 \times 10^4$.

Grid size	C_D
2.57×10^6	1.582
5.68×10^6	1.518
9.35×10^6	1.443
18.28×10^6	1.430

Reynolds number. With respect to the results in Table 1, due to the considerable computer capacity, analyses were performed with 9.3 million grid numbers for all Reynolds numbers.

In the LES turbulence model, the law-of-the-wall approach is applied using the wall boundary condition. The first cell from a no-slip wall is the symbolized dimensionless distance y^+ and is characterized as:

$$y^+ = \frac{\sqrt{\tau_w/\rho y}}{v} \tag{10}$$

In this equation, τ_ω and y express the shear stress and first cell height, respectively. In the current study, y^+ has ranged from 0.83 to 1.72. It is generally accepted that y^+ should be less than 1 ($y^+ < 1$) for most usage at low-Reynolds numbers, as given by Stringer et al. [36]. However, a study was completed at a high Reynolds number by Jagadeesh and Murali [37], who concluded that the mesh structure of $y^+ < 2$ with 5 cells in the boundary layer was sufficient to obtain correct results.

3. Results and discussion

The flow patterns obtained by experimental and numerical analyses around the equilateral triangular cylinder are compared at Re $= 2.9 \times 10^3$, Re $= 5.8 \times 10^3$ and Re $= 1.16 \times 10^4$ in Figs. 4–12. The dimensions of all images were normalized with the characteristic edge length of the triangle as *x/L* and *y/L*. The maximum and minimum values are given as a legend bar for the contours in each figure. The positive layers of the flow patterns are displayed as continuous line contours with a red background color, while the negative layers are displayed as dashed line contours with a blue background color.

3.1. Flow characteristics for instantaneous and time-averaged vorticity contours

The instantaneous and time-averaged vorticities were normalized with L/U_∞. In Fig. 4, the instantaneous vorticity ($\omega^* = \omega L/U_\infty$) results clarify the von Karman vortex shedding. PIV and LES results show that flow separation occurs from sharp-tip corners for all Reynolds numbers. Because of the shear layers, flow motion to the back of the equilateral triangular cylinder coming from the upper edge slants to the clockwise direction, while flow around the lower edge of the body rotates in the counter clockwise direction. After the separation of the flow from the body surface, small scale eddies roll up to form in the wake region. The Reynolds number plays an important role in the flow structure. Instantaneous vorticity patterns decrease in the formation length of the large-scale Karman vortex with increasing Reynolds number. However, these patterns are not clearly observed because of the closer values of the Reynolds number. Although the PIV and LES results are in good agreement in terms of instantaneous vorticity structure, the agreement of PIV and LES results clearly seems to be better for time-averaged vorticity patterns ($< \omega^* = \omega L/U_\infty >$) with maximum and minimum values in Fig. 5. Concerning the beginning and improvement of small-scale vorticity structures in the separating shear layer, the small clusters of vorticity concentration are not visible in the patterns of instantaneous vorticity for all Reynolds numbers in Fig. 4. The minimum positive and negative values of the vorticity contours were
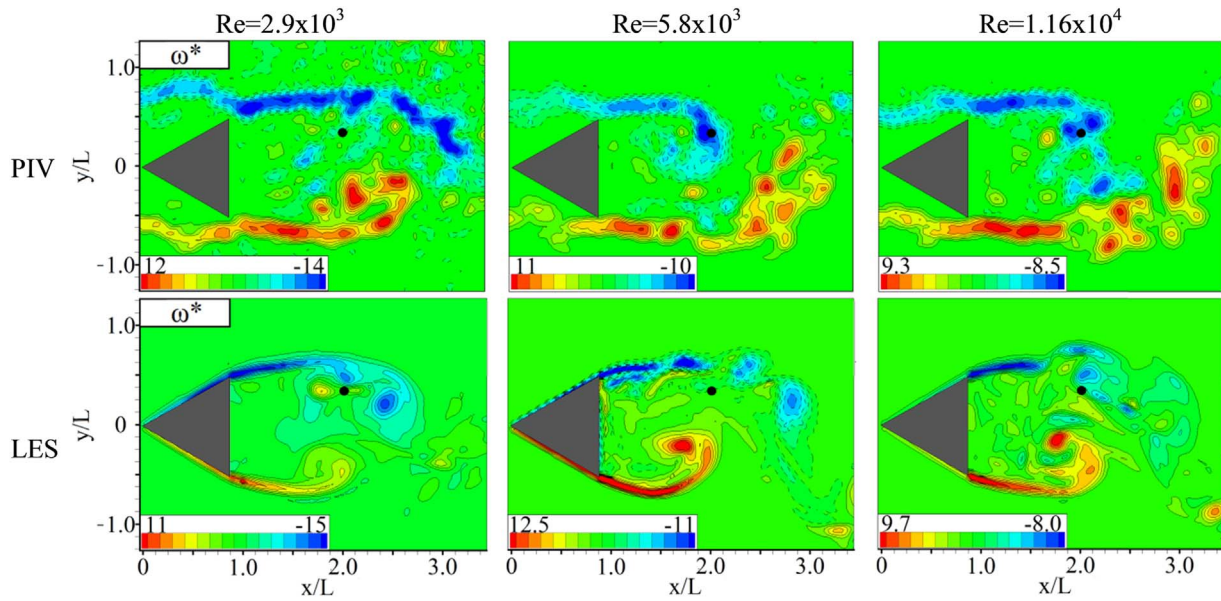
Fig. 4. Comparison of the normalized experimental and numerical instantaneous vorticity (ω^*) around the equilateral triangular cylinder.

observed near the symmetry plane, which is definition of vortex formation length, at Reynolds numbers of 2.9×10^3, 5.8×10^3 and 1.16×10^4. The form of the vorticity contours in the near-wake is similar for all Reynolds numbers. A large-scale vortex occurs in the downstream for $Re = 2.9 \times 10^3$. While increasing the Reynolds number, it moves to the upstream and approaches the back side of the triangular cylinder. In addition, in the part of the downstream region of the triangle, the time-averaged vorticity patterns are nearly equal to zero because the direction of the vortex shedding changes continuously. Therefore, the time-averaged vorticity patterns show that the von Karman Vortex Streets observed in the instantaneous vorticity images forming small-scale vortices have disappeared.

3.2. Comparison of streamline topology and the corresponding velocity contours

A reversed flow has occurred in the wake region as displayed by the velocity vectors ($< V >$) in Fig. 6. Velocity vectors with very small magnitude have been established in the wake region of the equilateral

triangular cylinder for all Reynolds numbers. However, the longer size of the velocity vectors can be observed along the shear layer. From $Re = 2.9 \times 10^3$ to $Re = 1.16 \times 10^4$, relatively longer velocity vectors were formed in the downstream of the body.

As emphasized in Fig. 5, from time-averaged vorticity patterns, the streamline patterns ($< \psi >$) of the triangular cylinder demonstrate that the flow structures in the wake region are almost equally symmetrical with respect to the centerline in Fig. 7. There are two symmetrical focus points F_1 and F_2 with a similar size and cycling in opposite directions, and a saddle point S (evident for intersections of streamlines) is formed clearly in the downstream of the wake. Saddle points in the wake region agree with the time-averaged vorticity contours in the PIV and LES results for all Reynolds numbers. The saddle point could also ensure a demonstration of the main formation length of the large-scale vortices. Saddle point distances normalized as x/L were approximately measured from the back side of the equilateral triangular cylinder at $Re = 2.9 \times 10^3$, $Re = 5.8 \times 10^3$ and $Re = 1.16 \times 10^4$ as 1.70/1.75, 1.65/1.70 and 1.60/1.65 by PIV/LES, respectively.

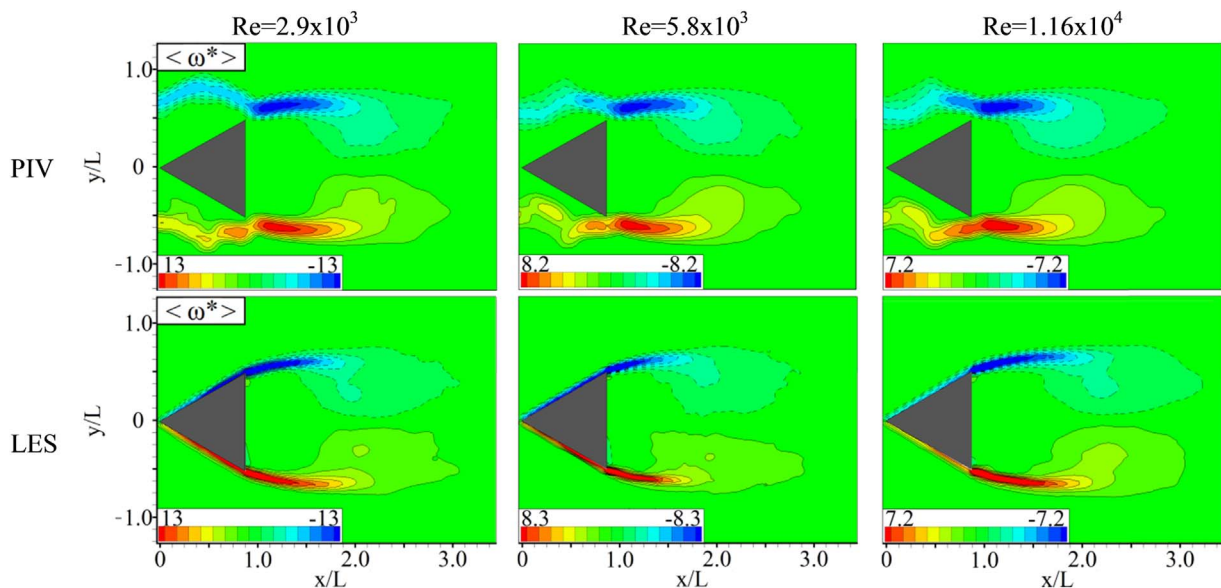The distributions of the dimensionless time-averaged streamwise

Fig. 5. Comparison of the normalized experimental and numerical time-averaged vorticity ($< \omega^* >$) around the equilateral triangular cylinder.

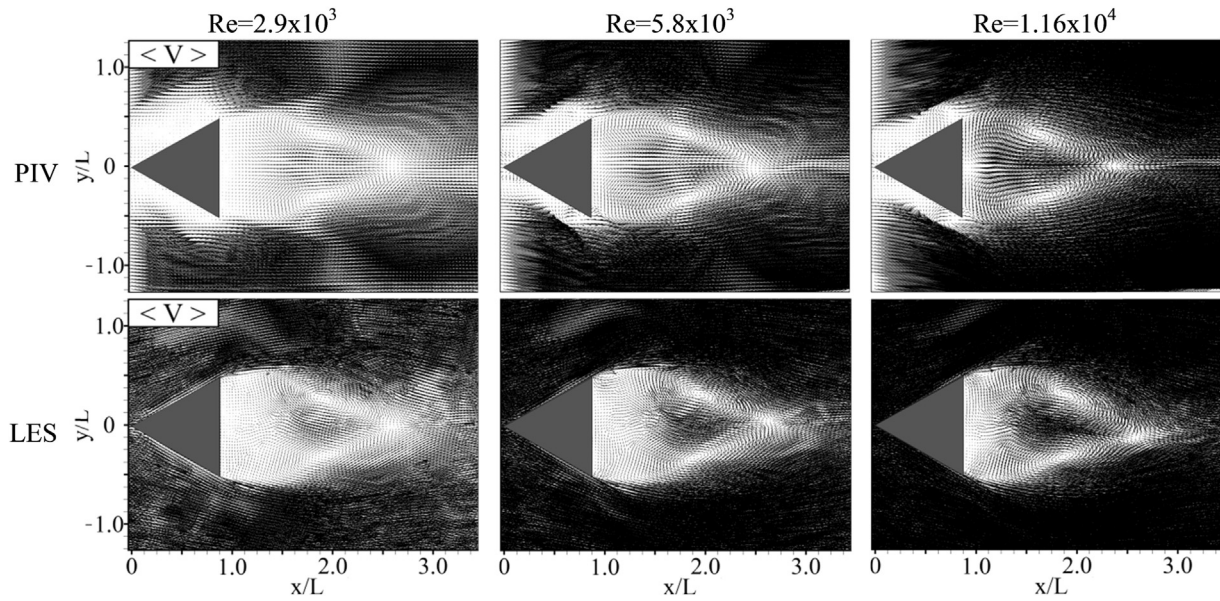**Fig. 6.** Comparison of the experimental and numerical velocity field ($< V >$) around the equilateral triangular cylinder.

velocity components ($< u^* = u/U_\infty >$) are illustrated in Fig. 8. Time-averaged streamwise velocity was normalized with free stream velocity (U_∞). Both PIV and LES results indicate the same minimum and maximum levels of the dimensionless values of streamwise velocity contours at $Re = 2.9 \times 10^3$, $Re = 5.8 \times 10^3$ and $Re = 1.16 \times 10^4$. The flow clearly accelerates after passing the sharp-tip corners and reaches the maximum value. The flow acceleration was observed in the region near the sharp-tip corners, and this region shrank due to the increase in the Reynolds number. It is also possible to describe the location of the stagnation point along the wake symmetry plane. From the PIV and the LES results, the distance from the rear surface of the triangle to the stagnation point at $Re = 2.9 \times 10^3$ is approximately *1.7L*. With increasing Reynolds number, the growth of the separated shear layers from the tip corner of the triangular cylinder shoulders is associated with a decrease in the wake size. Therefore, the location of the stagnation point approached the rear surface of the equilateral triangular cylinder and for PIV and LES results, indicated that the stagnation points are nearly 1.65*L* and 1.60*L* at $Re = 5.8 \times 10^3$ and $Re = 1.16 \times 10^4$, respec-

tively. Stagnation points can be attributed to the saddle (S) point from streamline topology in Fig. 7.

The time-averaged cross-stream velocity contours ($< v^* = v/U_\infty >$) are presented in Fig. 9. The time-averaged maximum positive and negative values of cross-stream velocity were observed on the upper and down sides of the equilateral triangular cylinder. The peaks of positive and negative values for PIV and LES increased with increasing Reynolds number. After the flow passing the equilateral triangular cylinder, two different pairs of clusters were developed in the downstream of the wake. The intersection of negative and positive cluster cross-stream velocity ($< v^* >$) in the wake of the equilateral triangular cylinder close to rear surface of the triangle have relatively larger values with increasing Reynolds numbers. From the PIV and LES results, the small size of the positive and large size of the negative cross-stream velocity contours are formed in the half-upper side of the wake region. In addition, just the opposite of this case is also formed in the half-lower side of the wake region for both Reynolds numbers along the axis line where there is a "switching" of the orientation from
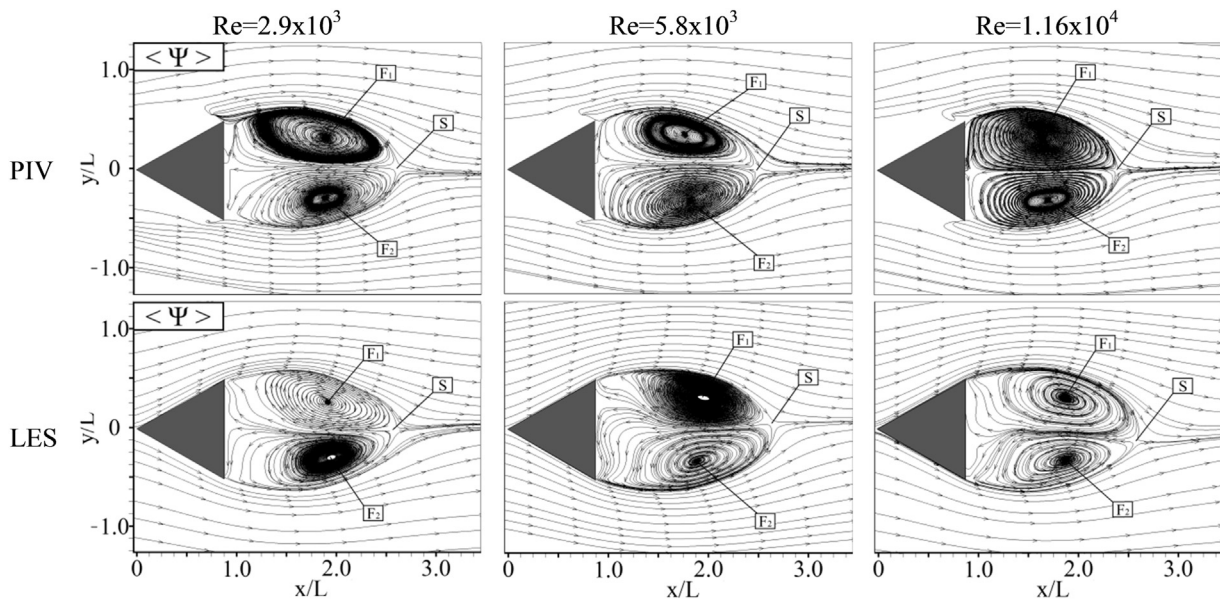

Fig. 7. Comparison of the experimental and numerical streamline topology ($< \psi >$) around the equilateral triangular cylinder.

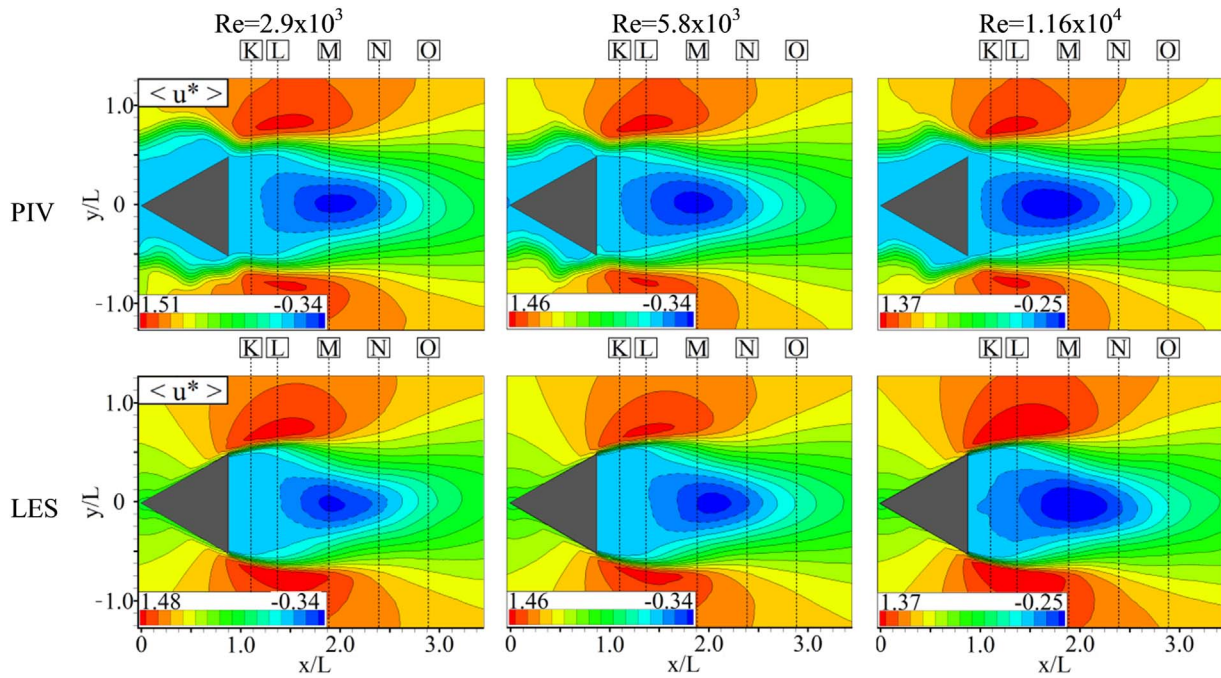**Fig. 8.** Comparison of the normalized experimental and numerical time-averaged streamwise velocity ($< u^* >$) around the equilateral triangular cylinder.

positive to negative values. The arrangement of the cross-stream velocity, ($< v^* >$), indicates two negative and positive peak points downstream of the equilateral triangular cylinder with the same intervals of PIV and LES results: $\pm$ 0.29 at Re = 2.9 × 10³, $\pm$ 0.36 at Re = 5.8 × 10³ and $\pm$ 0.38 at Re = 1.16 × 10⁴ demonstrate symmetrical flow structures in the wake region.

3.3. Variations of time-averaged fluctuating velocity patterns

The time-averaged normalized rms streamwise ($< u^*_{rms} = u_{rms}/U_\infty >$) and cross-stream wise velocity ($< v^*_{rms} = v_{rms}/U_\infty >$) are demonstrated in Figs. 10 and 11, respectively. They are not affected by Reynolds number and display nearly the same attitude for both PIV and LES results. In Fig. 10, rms streamwise velocity ($< u^*_{rms} >$) demonstrates that symmetrical double peaks are formed along the axis line in

the wake region for all cases that are placed nearly *1.15L* at Re = 2.9 × 10³, *1.275L* at Re = 5.8 × 10³ and *1.4L* at Re = 1.16 × 10⁴ for both experimental and numerical analyses. A possible explanation for these peak points can be related to the foci F_1 and F_2 (centers of vortices) regions in Fig. 7, where the streamwise velocity continuously fluctuates between the minimum and maximum values. The maximum values of rms cross-stream velocity are nearly same from the results of PIV and LES for each Reynolds number. Although double peaks occur for the rms streamwise velocity along the axis line, only one peak is demonstrated in the wake of the rms cross-stream velocity ($< v^*_{rms} >$) on the axis line in Fig. 11. The locations of peak points can be associated with the stagnation point in the wake of the equilateral triangular cylinder.
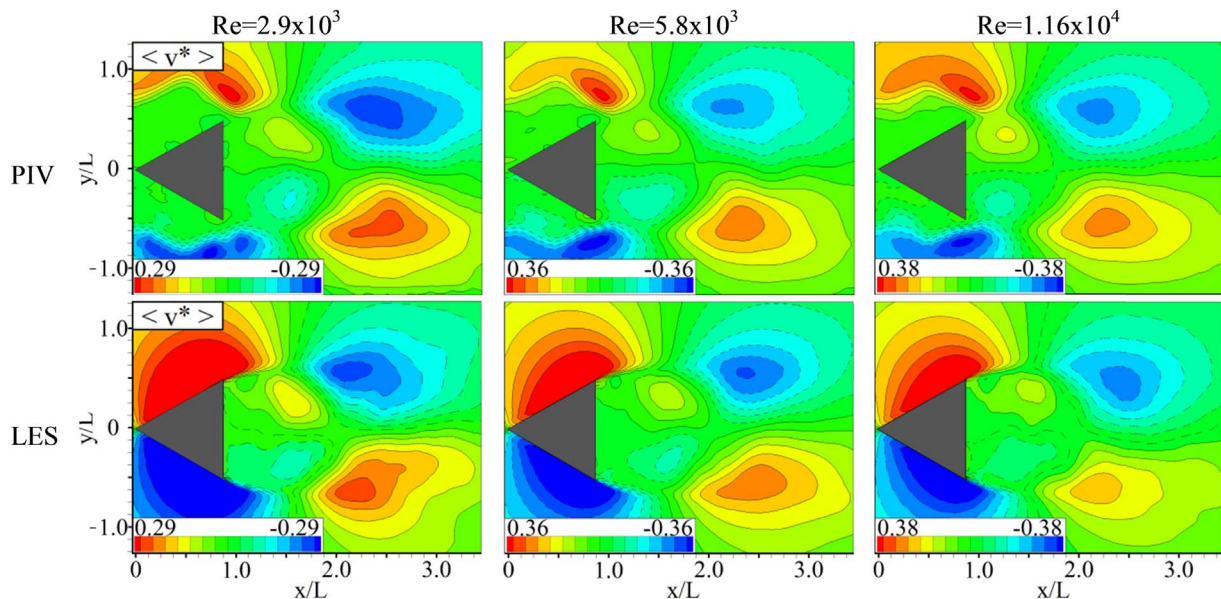

Fig. 9. Comparison of the normalized experimental and numerical time-averaged cross-stream velocity ($< v^* >$) around the equilateral triangular cylinder.

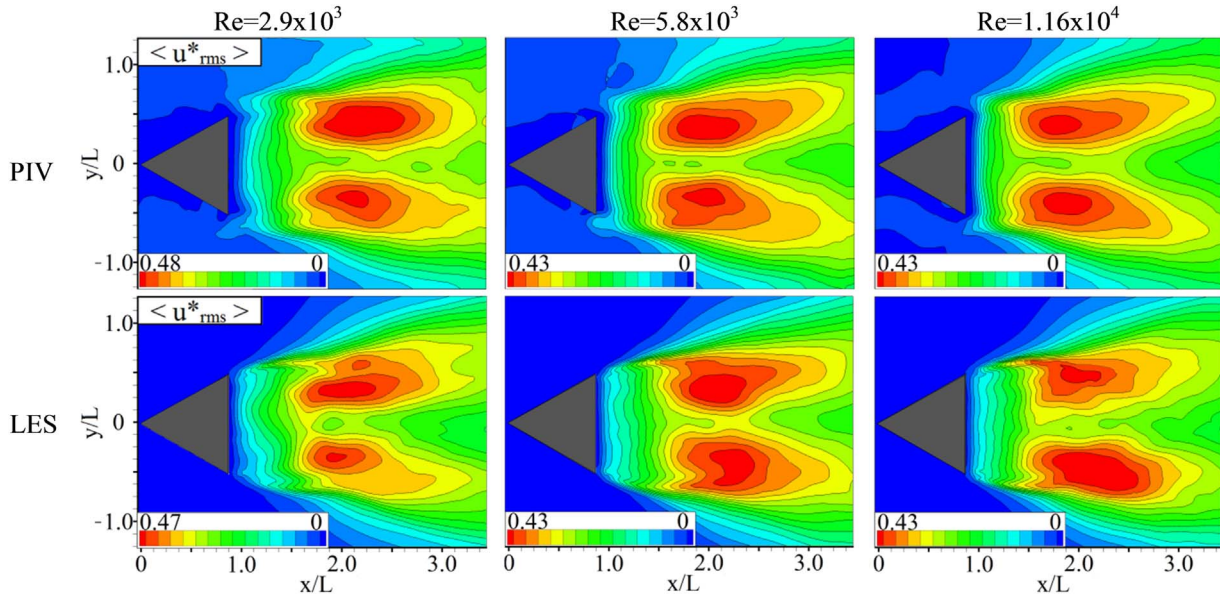**Fig. 10.** Comparison of the normalized experimental and numerical rms streamwise velocity fluctuations ($< u_{rms}^* >$) around the equilateral triangular cylinder.

3.4. Variations of Reynolds stress correlations

Reynolds stress correlations ($< u'v'/U_\infty^2 >$) indicate the comparison of momentum transfer at three Reynolds numbers for both analyses in Fig. 12. Two clusters with small and large scales are formed at Reynolds stress correlation images that are symmetrical along the axis line. The Reynolds stress correlations in and around the mean wake recirculation region are mainly because of the time-dependent behavior of the vortex shedding. In this context, as shown in time-averaged vorticity counters in Fig. 5, the Reynolds stress correlation is nearly zero in the outermost region of the flow fields. The small scaled clusters are positioned at the rear surface of the equilateral triangular cylinder and the large-scaled clusters occur on the back side of the small ones. Because of the fluctuations in the shear layers, the small-scale Reynolds stress region is close to the back side of the equilateral triangular cylinder which occurs because of the flow entrainment into the wake region. The similarity of the PIV and LES results shows that the center of the maximum negative and positive large-scaled clusters is placed

nearly *1.2L* in the wake region at Re = 2.9 × 10³, Re = 5.8 × 10³ and at Re = 1.16 × 10⁴. The large-scaled clusters moved further upstream and are positioned near to the base of the equilateral triangular cylinder with increasing Reynolds number. In addition to this movement, the positive and negative peak values decrease from ± 0.15 at Re = 2.9 × 10³ to ± 0.125 at Re = 5.8 × 10³. From Re = 5.8 × 10³ to Re = 1.16 × 10⁴, the peaks of negative and positive Reynolds stress have increased from ± 0.125 to ± 0.13.

3.5. Variations of time-averaged normalized streamwise velocity and Reynolds stress distributions along the vertical lines downstream of the equilateral triangular cylinder

Variations of the time-averaged streamwise velocity component ($< u^* >$) in Fig. 8 and Reynolds stress correlations ($< u'v'/U_\infty^2 >$) in Fig. 12 for all studied Reynolds numbers are described along the vertical stations as "K, L, M, N and O" which are *0.25L, 0.5L, 1.0L, 1.5L* and *2.0L,* respectively, away from the rear surface of the triangle along
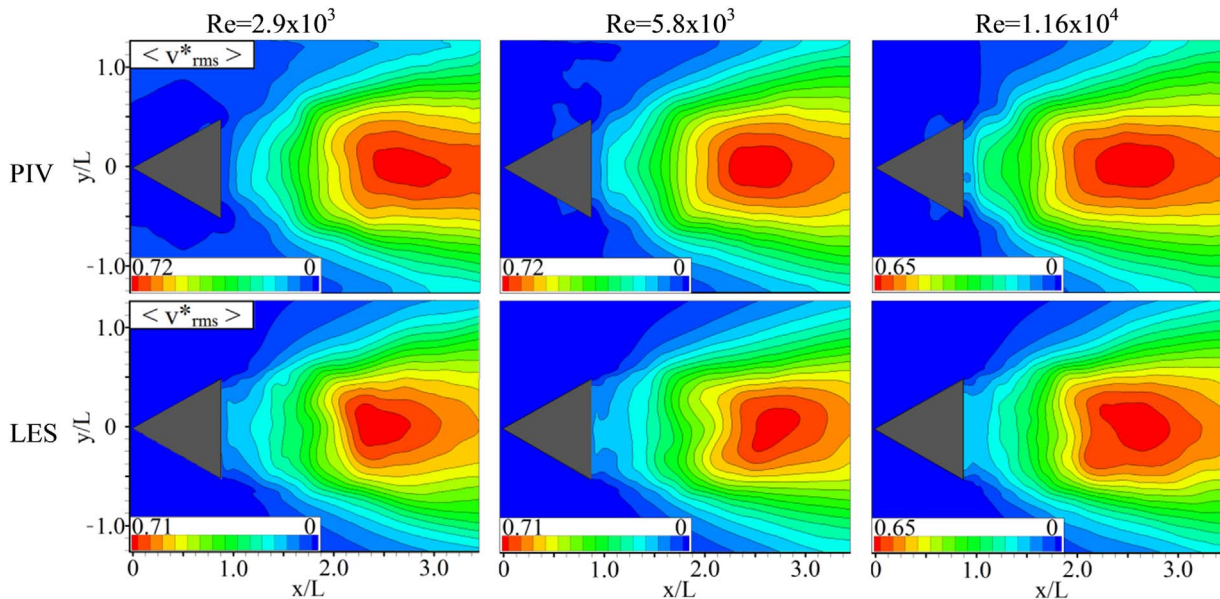

Fig. 11. Comparison of the normalized experimental and numerical rms cross-stream velocity fluctuations ($< v_{rms}^* >$) around the equilateral triangular cylinder.
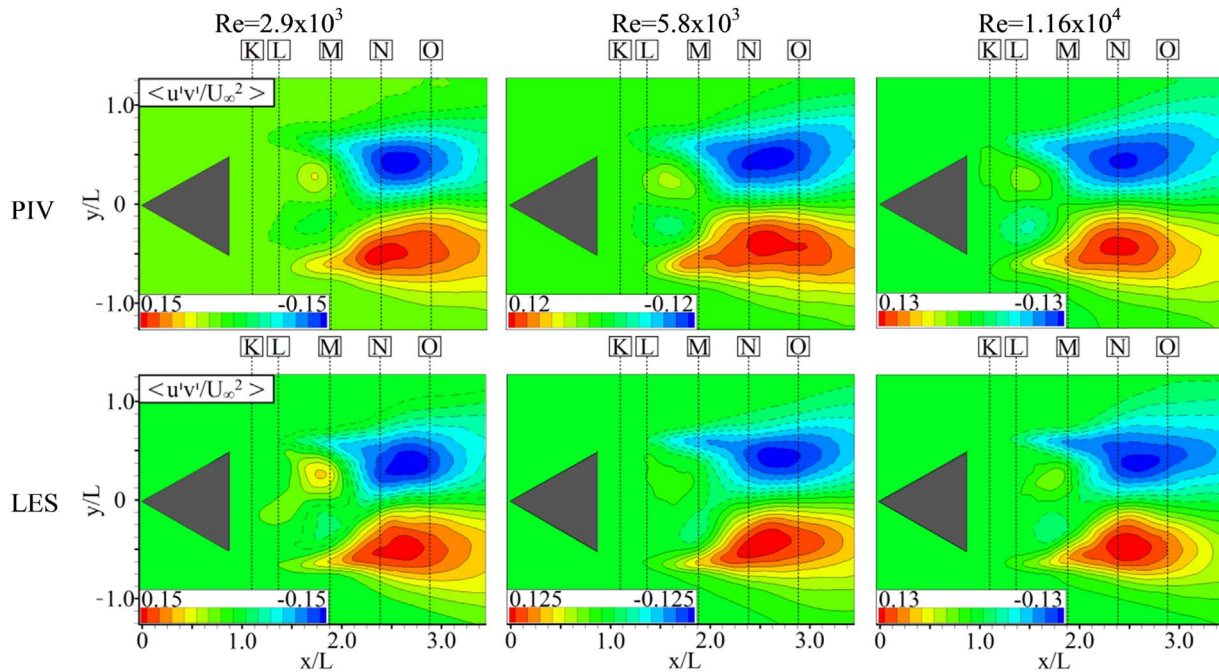
Fig. 12. Comparison of the normalized experimental and numerical Reynolds stress correlations ($< u'v'/U_\infty^2 >$) around the equilateral triangular cylinder.

the $+x$ axis. The distributions of the time-averaged streamwise velocity component ($< u^* >$) in Fig. 13 and the Reynolds stress correlations ($< u'v'/U_\infty^2 >$) in Fig. 14 are given downstream of the equilateral triangular cylinder for different cross-sections in the interval of *0.25L* to *2.0L*, the first row at Re = 2.9×10^3, the second row at Re = 5.8×10^3 and the bottom row at Re = 1.16×10^4. The red and blue lines represent the PIV and the LES results, respectively.

It is apparent that the streamwise velocities ($< u^* >$) are nearly zero in the shear layer between the back side of the equilateral triangular cylinder and the vertical station K for all Reynolds numbers. Because of the low-pressure region in the wake of the equilateral triangular cylinder, negative velocity components occur from station K to O, and the maximum negative values are obtained nearly at the vertical station of M for all Reynolds numbers. The experimental and numerical results demonstrate that the stagnation point in the wake of the triangle occurs between the stations of N and O for all Reynolds numbers, but it approaches the station N with increasing Reynolds numbers. The maximum values are reached at $y/L = \pm 0.6$ for vertical stations of K, L and M at all Reynolds numbers. However, values of streamwise velocities approach the uniform flow conditions at the vertical stations N and O at $y/L = \pm 0.6$ in Fig. 13. The minimum and maximum values of the time-averaged streamwise velocity and the distribution of its contour fields through the vertical lines for PIV are in close agreement with LES. Both methods clearly show the symmetrical flow structure in the wake region. Moreover, the difference between PIV and LES was found to be less than $\pm 5\%$ for the maximum values of streamwise velocity contours in Fig. 13.

As shown in Fig. 14, the Reynolds stress correlations ($< u'v'/U_\infty^2 >$) fluctuate due to small and large scaled clusters in the rear surface of the triangular cylinder. In Fig. 14, it is more visible that the small scaled clusters disappear after the station of M. Furthermore, the diminishing of the small scaled clusters occurs earlier along the vertical location of M at Re = 1.16×10^4 than at Re = 5.8×10^3. In the vertical direction after the location of approximately $y/L = \pm 0.7$, the values of the Reynolds stress correlations become zero for the examined flow field and Reynolds numbers. The Reynolds stress correlations downstream of the mean wake recirculation region occur mainly because of the time-dependent nature of the vortex shedding [3]. Therefore, the Reynolds stress correlations are zero along the symmetry axis because of the

symmetrical flow structure and achieve its maximum positive and negative values in the upper and lower regions of the axis line. For that reason, we can conclude that the Reynolds stress correlations are nearly zero in the free stream flow region. However, the Reynolds stress correlations obtain their maximum positive and negative values between the stations N and O associated with the rms of the velocity distributions in Figs. 10 and 11.

3.6. Spectral analysis and calculation of vortex shedding frequency

Mass flow rate measurement plays an important role in terms of scientific studies and industrial applications due to its stability under different temperature and pressure conditions compared to volume. Mass flow rate is also obtained from the multiplication of volumetric flow rate and fluid density. There are two options to attain the density. Fluid density is obtained with respect to measured medium conditions such as temperature, pressure etc. as a first option and a densitometer is considered for the second option. Nevertheless, the desired accuracy may not be provided as a result of the measurements. Although Coriolis and thermal flowmeters are utilized to measure the mass flow rate directly, these devices remain incapable for some practical applications. For this reason, the vortex shedding principle is accepted as an alternative method to measure the mass flow rate by using a vortex flowmeter. In this content, the vortex flowmeter benefits from a bluff body to generate the von Karman vortex shedding. In this study, an equilateral triangular cylinder model has been utilized as a bluff body or a vortex shedder, and flow around this geometry led to fluctuations in the wake region. Moreover, these fluctuations have certain frequency values with respect to flow conditions and these frequency values have been obtained both experimentally and numerically. Thus, the mass flow rate is defined by evaluating the frequency values.

In the present study, experimental and numerical results have been obtained and then compared. The vortex shedding frequency of the equilateral triangular cylinder has been attained with respect to the experimental and numerical results. The occurrence of the von Karman Vortex Street can be observed clearly the from instantaneous vorticity contours in Fig. 4. The dominant vortex shedding frequency f with the help of PSD is calculated from the time history of the streamwise velocity of the recorded PIV and LES data in the wake region of the
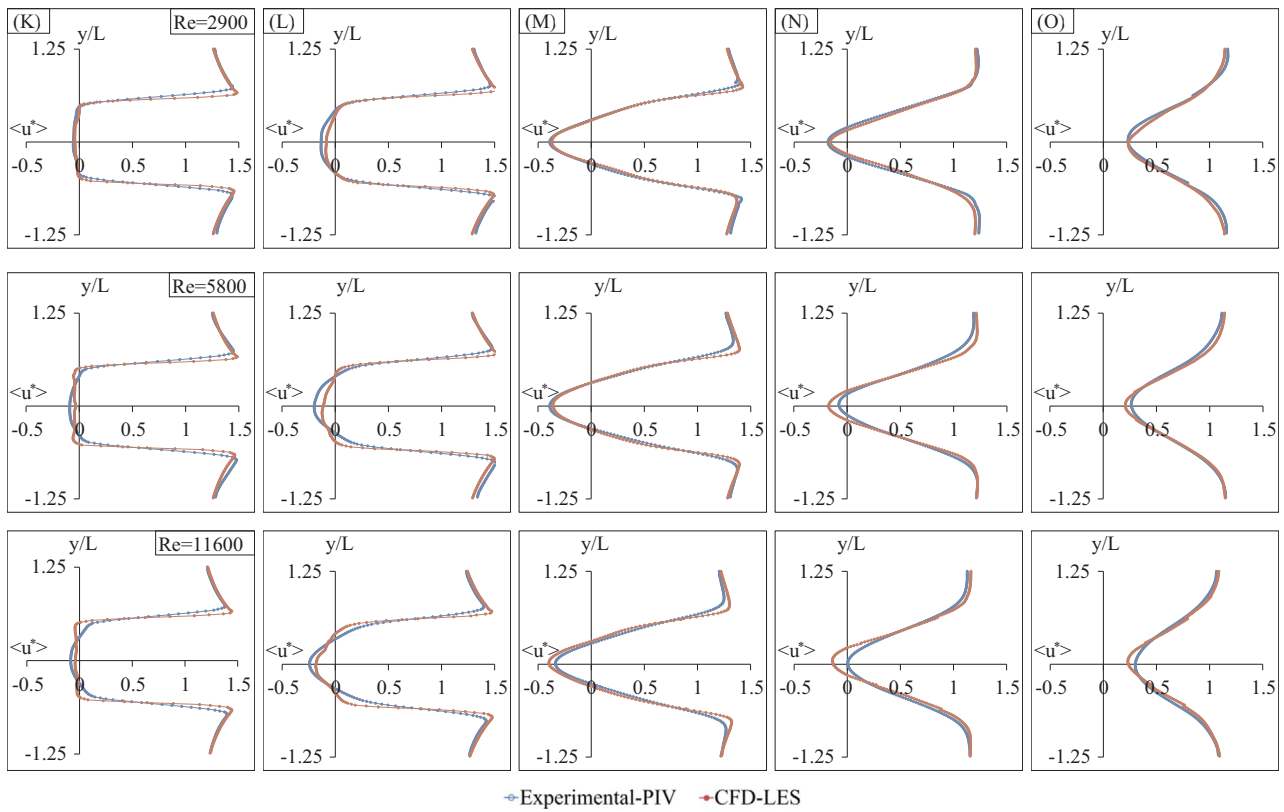
Fig. 13. Variations of the time-averaged streamwise velocity component ($< u^* >$) described along the vertical lines as "*K, L, M, N and O*", which are *0.25L, 0.5L, 1.0L, 1.5L* and *2.0L*, respectively, away from the rear surface of the equilateral triangular cylinder along the $+x$ axis.

Fig. 14. Variations of Reynolds stress correlations ($< u'v'/U_\infty^2 >$) described along the vertical lines as "*K, L, M, N and O*", which are *0.25L, 0.5L, 1.0L, 1.5L* and *2.0L*, respectively, away from the rear surface of the equilateral triangular cylinder along the $+x$ axis.
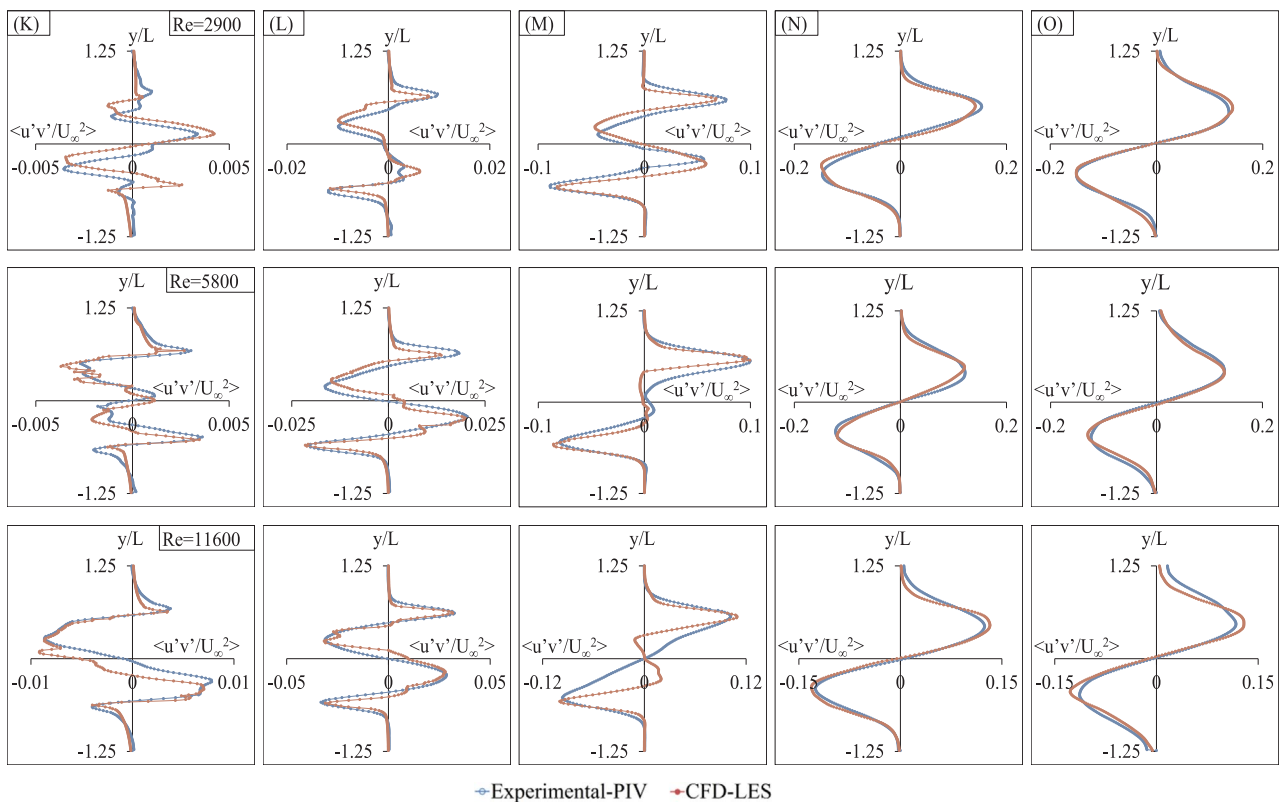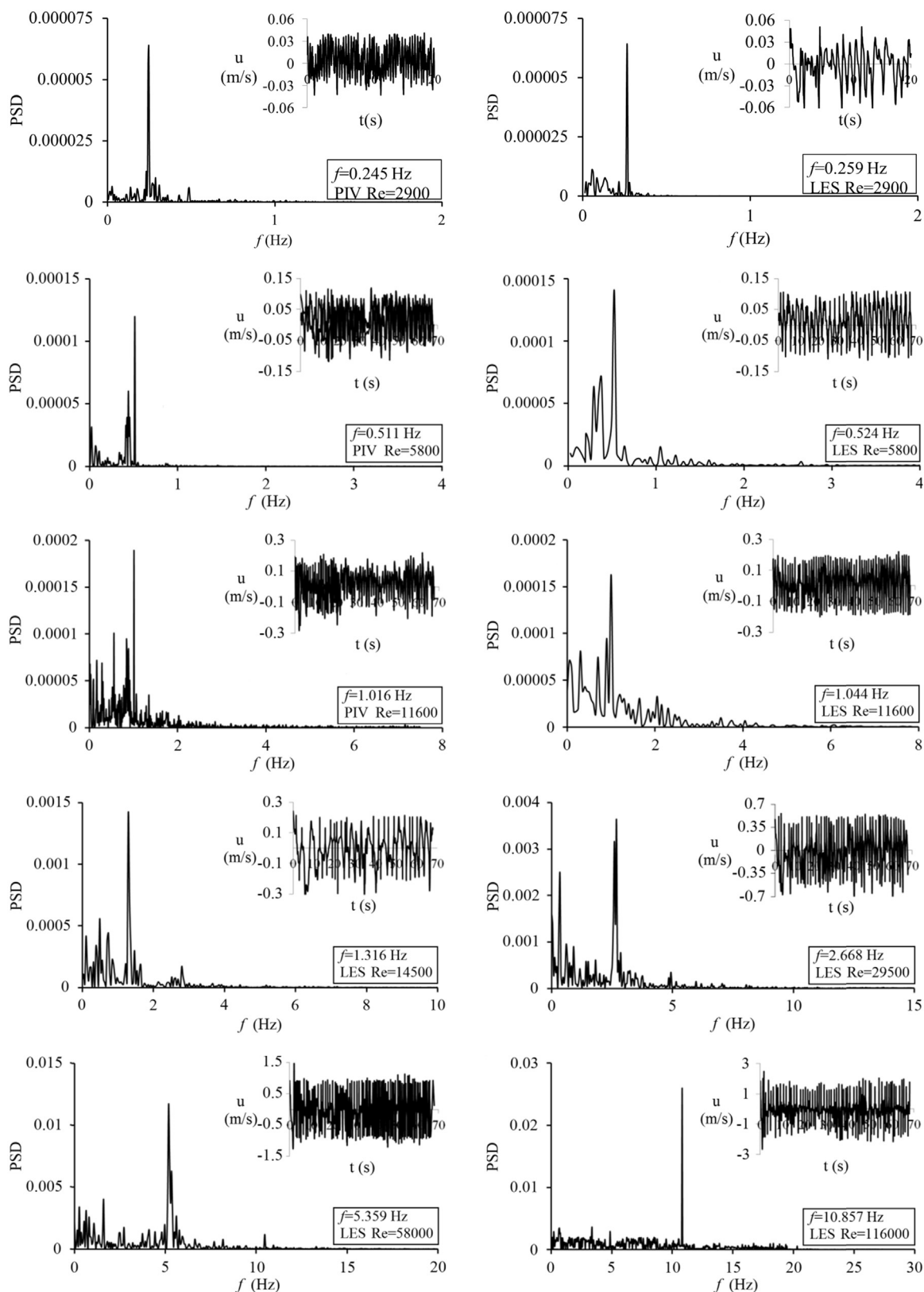
Fig. 15. Time history of instantaneous streamwise velocity component *u (m/s)* against *t (s)* and *Power Spectral Density (PSD) (m²/s)* analysis at the denoted point with black on the small image for all studied Reynolds numbers.

equilateral triangular cylinder, near the shear layer region denoted with a small black dot in Fig. 4.

In Fig. 15, the 1024 instantaneous streamwise velocity components were taken to obtain the dominant frequency by using spectral analysis, i.e., Fast Fourier Transformation (FFT). For FFT analyses, the input data number should be a power of 2. Instantaneous cross-stream velocities were also used to perform the FFT analyses, but the result was nearly the same as in the streamwise velocities. The streamwise velocity
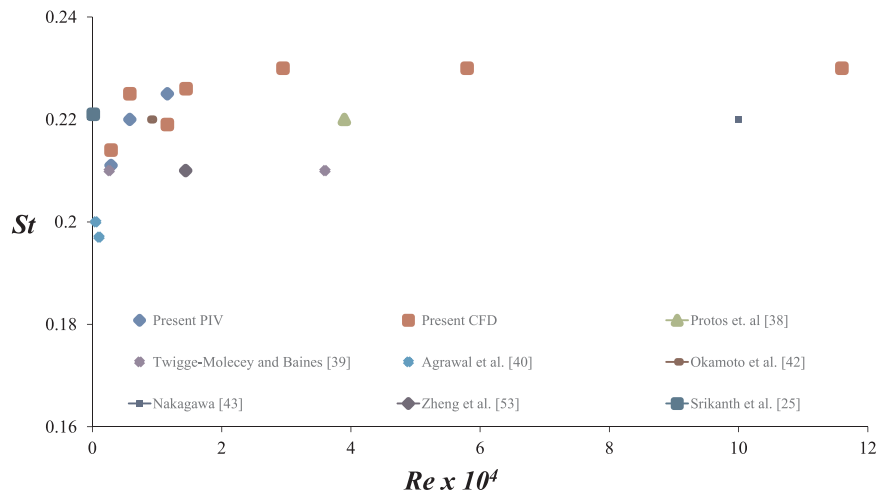
Fig. 16. Variation of Strouhal numbers with changing Reynolds numbers.

results are the only results given in the present study. FFT analyses reveal the vortex shedding frequency in the wake of the equilateral triangular cylinder, as shown in Fig. 15. The dominant vortex shedding frequency can be defined as the peak value of PSD, determined to be *0.245/0.259 Hz, 0.511/0.524 Hz* and *1.016/1.044 Hz* for PIV/LES at $Re = 2.9 \times 10^3$, $Re = 5.8 \times 10^3$ and at $Re = 1.16 \times 10^4$, respectively. This vortex shedding frequency, *f*, is a function of the Strouhal number, $St = (f L)/U_\infty$, and it is calculated as *0.211/0.214, 0.22/0.225* and *0.225/0.219* for PIV/LES results at $Re = 2.9 \times 10^3$, $Re = 5.8 \times 10^3$ and $Re = 1.16 \times 10^4$, respectively. Because the results obtained from PIV and LES were in agreement in terms of flow patterns and Strouhal numbers, the numerical analyses were also completed at the Reynolds numbers in the range of $2.9 \times 10^3 \leq Re \leq 1.16 \times 10^5$ to investigate the effect on the Strouhal number. The magnitudes of the spectral peak variation with the Reynolds number are illustrated in Fig. 15. With an increase in the Reynolds number, the PSD and vortex shedding frequency were also increased. However, the Strouhal number was not affected significantly by the change in the Reynolds number in the range examined. Comparison of the present study with the literature in terms of the Strouhal numbers against Reynolds number is given in Fig. 16. The Strouhal numbers in the related studies change approximately between $0.2 \leq St \leq 0.23$ in the wide range of the Reynolds numbers. When the Reynolds number increases, there is also an increment in the vortex shedding frequency to remain an almost constant value, as aforementioned. In addition, it is possible to associate the Strouhal number values with the Reynolds numbers investigated. Correlatively, Strouhal numbers obtained from both the experimental and numerical results remain almost constant due to the simultaneous rise in the velocity and the vortex shedding frequency. With this perspective, constancy in the Strouhal numbers presents an advantage as the vortex flowmeter and thus is utilized as a measurement device. In addition, the values of the Strouhal numbers and drag coefficients coincide with the values from literature summarized in Table 2.

3.7. Drag history of the equilateral triangular cylinder

One of the most important issues in studying flow over bluff bodies is related to the loading effect and the drag coefficient (C_D). In the present study, the flow characteristics and spectral analyses of flow around the equilateral triangular cylinder are given, in detail, by the PIV and LES results. The present PIV results are similar to the results of the LES analyses in terms of time-averaged flow field images and spectral analyses. Therefore, the drag coefficient is numerically calculated, due to the matching of flow characteristics. After forming the regular vortex shedding, the time-dependent drag coefficient at $Re = 5.8 \times 10^3$ was derived in Fig. 17. The drag coefficient fluctuates

Table 2

Comparison of the drag coefficients and Strouhal numbers with the literature.

| *Authors*	*Re*	C_D	*St*
Rasool et al. [39]	100 and 150	1.7 and 2.0	0.204 and 0.225
Srikanth et al. [40]	150	1.93	0.221
De and Dalal [41]	150	1.87	0.225
Chatterjee and Mondal [38]	150	1.904	0.203
Dhiman and Shyam [1]	150	1.894	0.204
Ganga Prasath et al. [42]	200	1.43	0.201
Bovand et al. [43]	200	1.91	0.193
Agrawal et al. [44]	520 and 1.04×10^3	0.65 and 2.47	0.20 and 0.197
Twigge-Molecey and Baines [45]	2.6×10^3 and 3.6×10^4	–	0.21
Present paper (experimental)	*2.9×10^3 to 1.16×10^4*	–	*0.211–0.225*
Present paper (numerical)	*2.9×10^3 to 1.16×10^5*	*1.43–1.33*	*0.214–0.23*
Okamoto et al. [46]	9×10^3	1.4	0.22
Zheng et al. [47]	14440	–	0.21
Protos et al. [48]	3.9×10^4	–	0.22
Obara and Matsudaira [49]	7.5×10^4	–	0.26
Nakagawa [50]	10^5	–	0.22
Venugopal et al. [19]	1.3×10^5 and 2.2×10^5	–	0.20
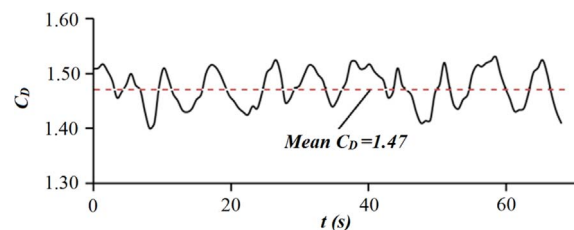
Fig. 17. The time history of drag coefficient at $Re = 5.8 \times 10^3$.

due to the vortex shedding in the shear layer. The time-averaged drag coefficient value was determined as $C_D = 1.47$ at $Re = 5.8 \times 10^3$. Alteration of the mean drag coefficient with the Reynolds number is shown in Fig. 18. The drag coefficient tends to increase from $Re = 2.9 \times 10^3$ to $Re = 5.8 \times 10^3$ as determined by the study. Accordingly, the same trend in increasing drag coefficients has also been observed in the study prepared by Chatterjee and Mondal [38] at lower Reynolds numbers. They have also studied the equilateral triangular cylinder in cross flow at low Reynolds numbers and obtained the following results: $C_D = 1.5334, 1.7546$ and 1.9037 at $Re = 50, 100$ and 150, respectively.
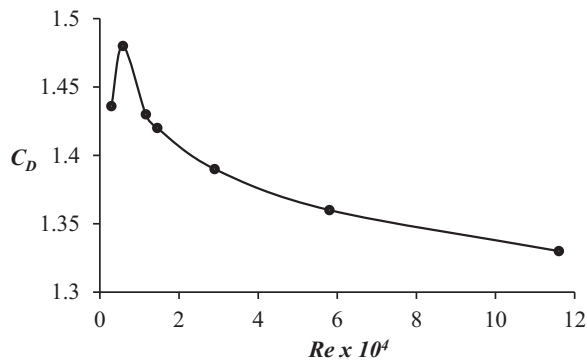
Fig. 18. Alteration of drag coefficient obtained by CFD for the different Reynolds numbers.

However, with the increase in the Reynolds number, the mean drag coefficient drops after the critical Reynolds number of $Re = 5.8 \times 10^3$. The drag coefficient as a term consists of the pressure (form) drag coefficient and the friction (viscous) drag coefficient. The friction drag coefficient is under the influence of the shear caused by the fluid, and the friction drag coefficient is more important for laminar flow conditions while the pressure drag coefficient is related to the pressure difference between the upstream and downstream area of the body, and it is more significant in turbulent flow conditions. For this reason, when the Reynolds number rises, the fluid flow approaches the turbulent flow or exceeds the critical value and becomes completely turbulent. In this way, the pressure drag coefficient becomes more important than the friction drag coefficient in terms of flow characteristics. With the increasing turbulence level of the flow, the wake region of the body shrinks and then becomes closer to the body. The smaller size of the wake region for the body means that there is less pressure difference between the upstream and downstream areas of the body. Therefore, less pressure difference constitutes less drag for the body since the pressure drag coefficient is more dominant under these conditions. The drag coefficient seems to be less affected at high Reynolds numbers and is going to be an asymptotic trend.

4. Conclusions

Numerical and experimental flow characteristics around the equilateral triangular cylinder have been obtained and compared by using the PIV and the LES methods. The present paper has supported quantitative experimental and numerical information in the near wake region of the equilateral triangular cylinder. In general, the comparative results of PIV and LES are quite similar in terms of flow characteristics and spectral analyses.

The time-averaged flow fields show symmetrical flow patterns occurring along the axis line of the equilateral triangular cylinder. With the increase in the Reynolds number, the wake of the equilateral triangular cylinder shrinks, and the stagnation points approach the back side of the triangular cylinder for both methods. The Strouhal numbers are nearly $St = 0.22$ for PIV and LES at all Reynolds numbers, and it can be inferred that these values are independent of the Reynolds number. However, the PSD and the vortex shedding are functions of the Reynolds number, and they increase with increasing Reynolds number. The drag coefficient is also obtained numerically and after $Re = 5.8 \times 10^3$, the drag coefficient displays a decreasing trend. In addition, it should be emphasized that the cell volume size is an important function to decide filtering operations for small scale eddies in the LES method. Therefore, to obtain accurate results using LES, the fine grid system must be created with a small grid that can result in increasing the solution time and thus requiring a powerful computing capacity. Comparison of the streamwise velocity and the Reynolds Stress correlation along the vertical lines in the wake region of the

equilateral triangular cylinder between the PIV and the LES yields a relative error less than ± 5%, which is quite acceptable. In the design and the manufacturing processes of different vortex flowmeters for industrial applications, using the PIV technique or the LES method saves time and cost.

References

[1] A. Dhiman, R. Shyam, Unsteady heat transfer from an equilateral triangular cylinder in the unconfined flow regime, Int. Sch. Res. Netw. Mech. Eng. 2011 (2011) 776–789, http://dx.doi.org/10.5402/2011/932738.

[2] X. Zhang, P. Blair, Turbulent vortex shedding from triangular cylinder using the turbulent body force potential model, in: Proceedings of the ASME 2000 Fluids Engineering Division Summer Meeting, Boston, MA, USA FEDSM2000-11172, 2000.

[3] M. Ozgoren, Flow structure in the downstream of square and circular cylinders, Flow Meas. Instrum. 17 (4) (2006) 225–235, http://dx.doi.org/10.1016/j.flowmeasinst.2005.11.005.

[4] A. Okajima, Strouhal numbers of rectangular cylinders, J. Fluid Mech. 123 (1982) 379–398, http://dx.doi.org/10.1017/S0022112082003115.

[5] D.T. Knauss, J.E.A. John, C.H. Marks, The vortex frequencies of bluff cylinders at low Reynolds numbers, J. Hydronautics 10 (4) (1976) 121–126, http://dx.doi.org/10.2514/3.48149.

[6] S.C. Yen, C.W. Yang, Flow patterns and vortex shedding behavior behind a square cylinder, J. Wind Eng. Ind. Aerodyn. 99 (2011) 868–878, http://dx.doi.org/10.1016/j.jweia.2011.06.006.

[7] M. Ozgoren, E. Pinar, B. Sahin, H. Akilli, Comparison of flow structures in the downstream region of a cylinder and sphere, Int. J. Heat Fluid Flow 32 (6) (2011) 1138–1146, http://dx.doi.org/10.1016/j.ijheatfluidflow.2011.08.003.

[8] R.F. Huang, B.H. Lin, S.C. Yen, Time-averaged topological flow patterns and their influence on vortex shedding of a square cylinder in cross-flow at incidence, J. Fluids Struct. 26 (2010) 406–429, http://dx.doi.org/10.1016/j.jfluidstructs.2010.01.003.

[9] F. Gu, J.S. Wang, X.Q. Qiao, Z. Huang, Pressure distribution, fluctuating forces and vortex shedding behaviour of circular cylinder with rotatable splitter plates, J. Fluids Struct. 28 (2012) 263–278, http://dx.doi.org/10.1016/j.jfluidstructs.2011.11.005.

[10] S.J. Lee, J.Y. Lee, PIV measurements of the wake behind a rotationally oscillating circular cylinder, J. Fluids Struct. 24 (2008) 2–17, http://dx.doi.org/10.1016/j.jfluidstructs.2007.06.001.

[11] A. Kalmbach, M. Breuer, Experimental PIV/V3V measurements of vortex-induced fluid structure interaction in turbulent flow—A new benchmark FSI-PfS-2a, J. Fluids Struct. 42 (2013) 369–387, http://dx.doi.org/10.1016/j.jfluidstructs.2013.07.004.

[12] S. Gunes, V. Ozceyhan, O. Buyukalaca, Heat transfer enhancement in a tube with equilateral triangle cross sectioned coiled wire inserts, Exp. Therm. Fluid Sci. 34 (6) (2010) 684–691, http://dx.doi.org/10.1016/j.expthermflusci.2009.12.010.

[13] N. Agrawal, S. Dutta, B.K. Gandhi, Experimental investigation of flow field behind triangular prisms at intermediate Reynolds number with different apex angles, Exp. Therm. Fluid Sci. 72 (2016) 97–111, http://dx.doi.org/10.1016/j.expthermflusci.2015.10.032.

[14] S. El-Sherbiny, Flow separation and reattachment over the sides of a 90° triangular prism, J. Wind Eng. Ind. Aerodyn. 11 (1–3) (1983) 393–403, http://dx.doi.org/10.1016/0167-6105(83)90116-2.

[15] G.V. Iungo, G. Buresti, Experimental investigation on the aerodynamic loads and wake flow features of low aspect-ratio triangular prisms at different wind directions, J. Fluids Struct. 25 (7) (2009) 1119–1135, http://dx.doi.org/10.1016/j.jfluidstructs.2009.06.004.

[16] J. Peng, X. Fu, Y. Chen, Experimental investigations of Strouhal number for flows past dual triangulate bluff bodies, Flow Meas. Instrum. 19 (6) (2008) 350–357, http://dx.doi.org/10.1016/j.flowmeasinst.2008.05.002.

[17] H. Zhang, Y. Huang, Z. Sun, A study of mass flow rate measurement based on the vortex shedding principle, Flow Meas. Instrum. 17 (1) (2006) 29–38, http://dx.doi.org/10.1016/j.flowmeasinst.2005.08.002.

[18] M. Cheng, G.R. Liu, Effects of after body shape on flow around prismatic cylinders, J. Wind Eng. Ind. Aerodyn. 84 (2) (2000) 181–196, http://dx.doi.org/10.1016/S0167-6105(99)00050-1.

[19] A. Venugopal, A. Agrawal, S.V. Prabhu, Influence of blockage and shape of a bluff body on the performance of vortex flowmeter with wall pressure measurement, Measurement 44 (5) (2011) 954–964, http://dx.doi.org/10.1016/j.measurement.2011.02.015.

[20] H.A. Khaledi, H.I. Andersson, On vortex shedding from a hexagonal cylinder, Phys. Lett. A 375 (2011) 4007–4021, http://dx.doi.org/10.1016/j.physleta.2011.09.046.

[21] J. Wang, J. Piechna, N. Müller, A novel design of composite water turbine using CFD, J. Hydrodyn. Ser. B 24 (1) (2012) 11–16, http://dx.doi.org/10.1016/S1001-6058(11)60213-8.

[22] B. Saavedra-Moreno, S. Salcedo-Sanz, A. Paniagua-Tineo, L. Prieto, A. Portilla Figueras, Seeding evolutionary algorithms with heuristics for optimal wind turbines positioning in wind farms, Renew. Energy 36 (11) (2011) 2838–2844, http://dx.doi.org/10.1016/j.renene.2011.04.018.

[23] R. Hassanzadeh, B. Sahin, M. Ozgoren, Large eddy simulation of free-surface effects on the wake structures downstream of a spherical body, Ocean Eng. 54 (1) (2012) 213–222, http://dx.doi.org/10.1016/j.oceaneng.2012.07.011.

[24] G. Hu, K.T. Tse, K.C.S. Kwok, Y. Zhang, Large eddy simulation of flow around an inclined finite square cylinder, J. Wind Eng. Ind. Aerodyn. 146 (2015) 172–184, http://dx.doi.org/10.1016/j.jweia.2015.08.008.

[25] K. Luo, S. Zhang, Z. Gao, J. Wang, L. Zhang, R. Yuan, J. Fan, K. Cen, Large-eddy simulation and wind-tunnel measurement of aerodynamics and aeroacoustics of a horizontal-axis wind turbine, Renew. Energy 77 (2015) 351–362, http://dx.doi.org/10.1016/j.renene.2014.12.024.

[26] H. Zhang, J. Yang, L. Xiao, H. Lu, Large-eddy simulation of the flow past both finite and infinite circular cylinders at Re=3900, J. Hydrodyn. Ser. B 27 (2) (2015) 195–203, http://dx.doi.org/10.1016/S1001-6058(15)60472-3.

[27] R.J. Adrian, Particle-imaging techniques for experimental fluid mechanics, Annu. Rev. Fluid Mech. 23 (1991) 261–304, http://dx.doi.org/10.1146/annurev.fl.23.010191.001401.

[28] A. Fouras, J. Soria, Accuracy of out-of-plane vorticity measurements derived from in-plane velocity field data, Exp. Fluids 25 (5) (1998) 409–430, http://dx.doi.org/10.1007/s003480050248.

[29] D.P. Hart, PIV error correction, Exp. Fluids 29 (1) (2000) 13–22, http://dx.doi.org/10.1007/s003480050421.

[30] Anonymous, Fluent 14.0 User Guide, Fluent Inc., 2013.

[31] J. Taghinia, M.M. Rahman, T. Siikonen, Large eddy simulation of flow past a circular cylinder with a novel sub-grid scale model, Eur. J. Mech. – B/Fluids 52 (2015) 11–18, http://dx.doi.org/10.1016/j.euromechflu.2015.02.001.

[32] C. Liang, G. Papadakis, Large eddy simulation of pulsating flow over a circular cylinder at subcritical Reynolds number, Comput. Fluids 36 (2) (2007) 299–312, http://dx.doi.org/10.1016/j.compfluid.2005.10.004.

[33] A.R. Vasel-Be-Hagh, R. Carriveau, D.S.K. Ting, Numerical simulation of flow past an underwater energy storage balloon, Comput. Fluids 88 (15) (2013) 272–286, http://dx.doi.org/10.1016/j.compfluid.2013.09.017.

[34] J. Tu, D. Zhou, Y. Bao, Z. Han, R. Li, Flow characteristics and flow-induced forces of a stationary and rotating triangular cylinder with different incidence angles at low Reynolds numbers, J. Fluids Struct. 45 (2014) 107–123, http://dx.doi.org/10.1016/j.jfluidstructs.2013.11.004.

[35] S. Yagmur, S. Dogan, M.H. Aksoy, E. Canli, M. Ozgoren, Experimental and numerical investigation of flow structures around cylindrical bluff bodies, Eur. Phys. J. Conf. 92 (2015) 02113, http://dx.doi.org/10.1051/epjconf/20159202113.

[36] R.M. Stringer, J. Zang, A.J. Hillis, Unsteady RANS computations of flow around a circular cylinder for a wide range of Reynolds numbers, Ocean Eng. 87 (1) (2014) 1–9, http://dx.doi.org/10.1016/j.oceaneng.2014.04.017.

[37] P. Jagadeesh, K. Murali, Application of low-Re turbulence models for flow simulations past underwater vehicle hull forms, J. Nav. Archit. Mar. Eng. 2 (1) (2005) 41–54, http://dx.doi.org/10.3329/jname.v2i1.2029.

[38] D. Chatterjee, B. Mondal, Mixed convection heat transfer from an equilateral triangular cylinder in cross flow at low Reynolds numbers, Heat Transf. Eng. 36 (1) (2015) 123–133, http://dx.doi.org/10.1080/01457632.2014.906800.

[39] T. Rasool, A. Dhiman, M. Parveez, Cross-buoyancy mixed convection around a confined triangular bluff body, Numer. Heat Transf. Part A: Appl. 67 (4) (2015) 454–475, http://dx.doi.org/10.1080/10407782.2014.937250.

[40] S. Srikanth, A.K. Dhiman, S. Bijjam, Confined flow and heat transfer across a triangular cylinder in a channel, Int. J. Therm. Sci. 49 (2010) 2191–2200, http://dx.doi.org/10.1016/j.ijthermalsci.2010.06.010.

[41] A.K. De, A. Dalal, Numerical study of laminar forced convection fluid flow and heat transfer from a triangular cylinder placed in a channel, J. Heat Transf. 129 (5) (2006) 646–656, http://dx.doi.org/10.1115/1.2712848.

[42] S. Ganga Prasath, M. Sudharsan, V. Vinodh Kumar, S.V. Diwakar, T. Sundararajan, Shaligram Tiwari, Effects of aspect ratio and orientation on the wake characteristics of low Reynolds number flow over a triangular prism, J. Fluids Struct. 46 (2014) 59–76, http://dx.doi.org/10.1016/j.jfluidstructs.2013.12.008.

[43] M. Bovand, S. Rashidi, J.A. Esfahani, Enhancement of heat transfer by nano fluids and orientations of the equilateral triangular obstacle, Energy Convers. Manag. 97 (2015) 212–223, http://dx.doi.org/10.1016/j.enconman.2015.03.042.

[44] N. Agrawal, S. Dutta, B.K. Gandhi, An experimental study on flow past an equilateral prism at intermediate Reynolds number and the effect of its orientation, in: Proceedings of the ASME Fluids Engineering Division Summer Meeting, Incline Village, NV, USA (2013) FDSM2013-16474, 2013.

[45] C.F.M. Twigge-Molecey, W.D. Baines, Aerodynamic forces on a triangular cylinder, J. Eng. Mech. Div. 99 (4) (1973) 803–818.

[46] T. Okamoto, M. Yagita, K. Ohtsuka, Experimental investigation of the wake of a wedge, Bull. JSME 20 (141) (1977) 323–328, http://dx.doi.org/10.1299/jsme1958.20.323.

[47] Y. Zheng, A. Rinoshika, S. Fujimoto, Triangle cylinder wake analysis based on wavelet and POD techniques, Procedia Eng. 126 (2015) 108–112, http://dx.doi.org/10.1016/j.proeng.2015.11.188.

[48] A. Protos, V.W. Goldschmidt, G.H. Toebes, Hydroelastic forces on bluff cylinders, J. Basic Eng. 90 (3) (1968) 378–386, http://dx.doi.org/10.1115/1.3605111.

[49] H. Obara, Y. Matsudaira, Large vortex formation-mechanism behind wedge under several separation conditions, JSME Int. J. Ser. B Fluids Therm. Eng. 41 (4) (1998) 788–795, http://dx.doi.org/10.1299/jsmeb.41.788.

[50] T. Nakagawa, Vortex shedding mechanism from a triangular prism in a subsonic flow, Fluid Dyn. Res. 5 (2) (1989) 69–81, http://dx.doi.org/10.1016/0169-5983(89)90012-9.